




In vivo monitoring of vascularization and oxygenation of tumor xenografts using optoacoustic microscopy and diffuse optical spectroscopy

K. G. AKHMEDZHANOVA,^{1,2} A. A. KURNIKOV,¹  D. A. KHOCHENKOV,^{3,4} YU. A. KHOCHENKOVA,³ A. M. GLYAVINA,^{1,2} V. V. KAZAKOV,¹ A. V. YUDINTSEV,² A. V. MASLENNIKOVA,^{1,2} I. V. TURCHIN,¹ P. V. SUBOCHEV,¹ AND A. G. ORLOVA^{1,*}

¹*Institute of Applied Physics, Russian Academy of Sciences, Nizhny Novgorod, Russia*

²*Lobachevsky State University of Nizhny Novgorod, Nizhny Novgorod, Russia*

³*N.N. Blokhin National Medical Research Center of Oncology, Moscow, Russia*

⁴*Togliatti State University, Togliatti, Russia*

**ag.orlova@mail.ru*

Abstract: The research is devoted to comparison of the blood vessel structure and the oxygen state of three xenografts: SN-12C, HCT-116 and Colo320. Differences in the vessel formation and the level of oxygenation are revealed by optoacoustic (OA) microscopy and diffuse optical spectroscopy (DOS) respectively. The Colo320 tumor is characterized by the highest values of vessel size and fraction. DOS showed increased content of deoxyhemoglobin that led to reduction of saturation level for Colo320 as compared to other tumors. Immunohistochemical (IHC) analysis for CD31 demonstrates the higher number of vessels in Colo320. The IHC for hypoxia was consistent with DOS results and revealed higher values of the relative hypoxic fraction in Colo320.

© 2022 Optica Publishing Group under the terms of the [Optica Open Access Publishing Agreement](#)

1. Introduction

Features of tumor vascular bed directly determine the metabolism and oxygen supply. Oxygenation is one of the most important parameters of biological tissue. A lack of oxygen in the tumor provokes hyperexpression of angiogenic factors, prevents the normal development of blood vessels in the neoplasm, which leads to increased hypoxia and tissue necrosis [1].

Immature vessels of the newly formed bloodstream are characterized by a number of structural and functional anomalies. These vessels are highly tortuous and saccular. The vascular walls are highly permeable due to irregular coverage of the basement membrane, pericytes and tumor cells [2]. Such abnormal features of the tumor vascular network lead to impaired blood circulation in the tumor, reducing its supply of oxygen and nutrients, causing the induction of hypoxia and as a consequence prevent the accessibility of drugs to the tumor tissue and increase its resistance to therapy [3].

Neoangiogenesis and oxygen state of the tumor become two inseparably incorporated characteristics of the malignant process, which require simultaneous comprehensive study both for diagnostic purposes and for choosing the optimal path of treatment and evaluating its effectiveness. Each type of neoplasm is characterized by pathological features that determine the prognosis of the disease and different approaches to its therapy. Microvessel density as well as the level of expression of angiogenic factors were suggested to be a significant prognostic indicator [4–6]. To decide on the most appropriate tactics for clinical treatment and predict tumor development, it is necessary to study the structure of the vascular component of various neoplasms [4].

Traditionally immunohistochemical (IHC) analysis is used to study tumor vascularization *ex vivo* [7]. IHC allows counting microvascular density by specific markers of endothelial cells, but it is limited in assessing the vascular pattern of the entire tumor volume and unsuitable for real-time monitoring. Traditional non-invasive methods for *in vivo* study of the vascular bed such as angiography, dopplerography, magnetic resonance imaging, positron emission tomography, optical coherence tomography also have a number of limitations [8]. Diffuse optical spectroscopy (DOS) is based on detection of the multiply scattered diffuse component of light that has passed through a layer of biological tissue and reconstruction of the scattering and absorption coefficients of the tissue based on the results of these measurements. Since absorption spectra (μ_a) of the main tissue chromophores (oxy- (HbO₂) and deoxyhemoglobin (HHb)) are known, it is possible to determine their concentrations and indirectly calculate total hemoglobin (tHb) concentration and the level of tissue oxygen saturation (StO₂) [9,10]. DOS has found its applications both in experimental [11,12] and clinical oncology [13–15] primarily for assessment of tumor oxygenation and hemoglobin content.

Optoacoustic (OA) angiography is based on the registration of broadband ultrasound resulted from absorption of a pulsed light by molecules of hemoglobin contained in blood-filled areas. At the depth of the DOS study (in the visible wavelengths range - a few millimeters), the resolution of OA angiography reaches several tens of micrometers.

Multispectral OA scanning allows to highlight the contrast of various tissue chromophores, such as melanin or oxy/deoxy hemoglobin. Hybrid OA method is therefore suitable for solving the problems of clinical and experimental oncology both for the diagnosis of superficially located tumors [16–18] and for the studies of tumor models vascular pattern during growth and after the treatment [19,20].

In this work a comparison of the characteristics of the vascular network of experimental tumors of different morphogenesis was made using complementary OA and DOS methods. DOS was used to monitor changes in oxygenation and blood filling of neoplasms, and bright-field OA microscopy was used to assess changes in the structure of the bloodstream. Both OA and DOS experimental setups have been created by the group of authors previously and adapted for this study. The results of *in vivo* studies were confirmed using IHC analysis of tumor tissue samples for CD31 and hypoxia. The combination of methods made it possible to identify the features of blood vessel structure and their influence on oxygenation of various tumor models for the first time.

2. Method and materials

2.1. Animals and tumor models

The study was performed on Balb/c-nu/nu female mice, obtained from “Pushchino” animal farm (Moscow, Russia). Three tumor models based on cell lines of renal cell carcinoma SN-12C (n = 4) and colon cancer carcinoma cells HCT-116 (n = 4) and Colo320 (n = 4) were selected.

The animal studies were approved by the Ethics Committee of N.N. Blokhin National Medical Research Center of Oncology (Protocol No 04P, 29.07.2021). Tumor cells were injected subcutaneously into the thigh area at a concentration of 2×10^7 cells/ml with Matrigel (Corning, USA) in a ratio of 2:1.

The experiment was started on the 7th day after cells inoculation, when the tumor size reached at least 35 mm³ and continued until the volume of 700 mm³. Tumor node volume was calculated as $V = a \cdot b^2 / 2$, where V is the volume, a – length value, b – width value of the node. Tumor volume doubling time was determined as $(t_2 - t_1) \cdot \log_2 (V_2 / V_1)$ from 7 till 29 days of growth, where t_{1,2} are the days after tumor inoculation, V_{1,2} are tumor volumes on the corresponding days [21]. OA and DOS study was carried out every 7 days until the 29th day of growth for SN-12C, HCT-116, Colo320 and then with an interval of 12, 35, 49 days for SN-12C. OA and

DOS investigation of mouse normal tissues (skin and underlying muscle) were performed on the first day of experiment.

During OA and DOS investigation, animals were immobilized using an anesthesia and respiratory machine (Zoomed, Russia). Inhaling gas containing 1.5% Isoflurane (Laboratorios Karizoo, Spain) in 100% O₂ (gas flow rate 0.1 L/min) was supplied through the custom-made tubing (Fig. 1). The combination of gases used in our work changes tumor StO₂ insignificantly [22].

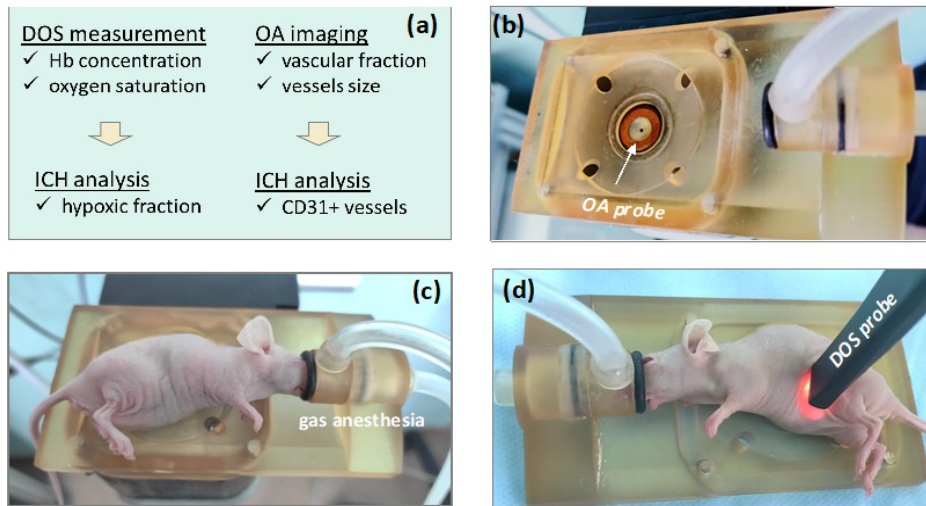


Fig. 1. Experimental design (a); anesthesia and positioning of the animal for OA and DOS studies: supporting plate with bright-field OA probe (b), Balb/c-nu/nu mouse during OA scanning (b), Balb/c-nu/nu mouse during DOS measurements (c)

2.2. OA setup

Scanning OA angiography system was based on [23] and consisted of two scanning stages (15×15 mm²; 15 μ m) triggering pulsed laser (532 nm; 1 ns; 2 kHz) and digitizer (16 bit; 200 MHz). A new bright-field probe (Fig. 1(b)) based on 400 μ m multimode optical fiber and custom-made [24] wideband [25] polyvinylidene difluoride (PVDF) detector providing less than 50 μ m lateral spatial resolution [26]. The scanning was performed inside immersion chamber (Fig. 1(c)) integrated with removable supporting plate (Fig. 1(d)) containing custom-made mask for gas anesthesia.

Each 3D dataset was processed by Matlab-based GUI interface implementing reconstruction sequence [27] consisting in \sim 1-80 MHz band-pass filtration [28] followed by delay-and-sum reconstruction in XZ and YZ planes [29]. No vessel-enhancement techniques were applied to OA data.

The reconstructed 3D OA datasets were plotted as maximum intensity projection (MIP) 2D images, which were then binarized and analyzed using ImageJ toolbox (NIH, USA) and the Particle Analysis toolbox. For the vessel analysis tumor zones were manually selected, at the outer boundary of the peripheral tumor vessel area. Threshold parameter was chosen to reduce the amount of background noise in binarized OA images. Vascular fraction was determined as a percentage of tumor area occupied by vessels in the OA images. The characteristic size of vessel segments was calculated by averaging individual vessel areas [20].

2.3. DOS setup

Reflection-mode DOS setup was based on the broadband LED source of probing radiation and the spectrometer [30]. The DOS fiber-optic probe consisting of three 400 micron fibers located in a line at a fixed distance of $d = 1.75$ mm from each other. One collection fiber and two source fibers provide two source-detector separations of 1.75 and 3.5 mm to perform calibration free measurements of optical attenuation spectrum by applying ratiometric approach. The optical probe was brought into direct contact with the biological tissue. Using the setup, the initial spectra of diffusely scattered radiation cross over through the tissues are obtained. Absorption coefficient, as well as concentrations of oxy-, deoxy-, total hemoglobin and blood oxygen saturation were reconstructed from the ratio of raw spectra obtained at different source-detector separations in the wavelength range of 520–590 nm [31]. The reconstruction procedure is based on a deep direct neural network, which consists of 6 layers and has 141987 parameters. To train the neural network 214220 spectra simulated from diffusion approximation of Radiative Transfer Equation for various component compositions were used. These spectra obtained under the assumption that all tissue chromophores except hemoglobin's have constant absorption in the spectral range 520-590 nm and the reduced scattering spectra has a power dependence on the wavelength. It was shown that such approach has less reconstruction error compared to traditional optimization applied in DOS [32].

2.4. Morphological study

IHC analysis was performed on the 29th day after inoculation of HCT-116, Colo320 cells and on the 125th day after inoculation of SN-12C cells. The hypoxia marker Pimonidazole hydrochloride (HPI, Inc., USA) was administered intraperitoneally at 60 mg/kg 45 min before sacrifice of mice. Excised tumors were cut into two parts. One half of tumors was then frozen in O.C.T. Compound (Sakura Finetek U.S.A., Inc., USA) and used for ICH hypoxia assay.

Detection of zones with a low oxygen state (< 10 mm Hg) was carried out using the marker pimonidazole and monoclonal antibodies with a Fluorescein isothiocyanate (FITC) fluorescent label (Hypoxyprobe, Inc., USA) on 7 μ m thickness sections. FITC fluorescence zones of the whole tumor section were visualized using a Carl Zeiss LSM 710 laser scanning microscope (LSM) (Carl Zeiss GmbH, Jena, Germany) at 10x magnification. FITC fluorescence was excited at a wavelength of 488 nm and registered in the range of 500-735 nm. The relative hypoxic fraction (RHF) was calculated as the percentage of pimonidazole-positive zones from the total area of the sample [33] using a Matlab. The threshold value of the FITC fluorescence intensity was chosen based on the signal from stained tumor sections without pre-accumulated pimonidazole. Areas of necrosis were excluded from the analysis [34].

The other half of the tumor was fixed in 10% formalin (Biovitrum, Russia) for 48 hours, then embedded in paraffin and cut into 4-5 μ m thick sections. After dewaxing and antigen retrieving, the sections were incubated with Peroxidase blocking solution (Abcam, UK). After 10 minutes they were washed in PBS and incubated with Protein blocking solution (Abcam, UK) for 15 minutes. Subsequently, the sections were incubated with antibodies to the mouse endothelial cell marker CD31 (Abcam, UK) in 1/50 dilution for 18-20 hours at 4°C, then washed twice in PBS and incubated with Biotinylated Goat Anti-Polyvalent Mouse and Rabbit (Abcam, UK) and streptavidin-HRP conjugate (Abcam, UK). After washing the samples twice with PBS, DAB Substrate Kit solution (Abcam, UK) was applied for 10 min; sections were washed in PBS and stained with Mayer's hematoxylin (Sigma, USA). Finally, the samples were washed in running water, dehydrated by sequentially passing through a series of xylene and ethanol solutions and were placed under a coverslip using a Thermo Shandon Mount (Thermo Fisher Scientific, USA). Microvessels stained for CD31 + were counted in 8 microscope fields per tumor at 200x magnification using Nikon Eclipse 80i microscope with Ds-Fi1 (Nikon, Japan); the values of their number were normalized to area.

2.5. Statistical analysis

All measurement data obtained for tumor volume were plotted as means \pm SD. For statistical analysis, the IBM SPSS Statistics software and BioStat Professional were used. One-way ANOVA with Bonferroni correction was performed to estimate the significance of the differences between tumor models in each time point and t-test for dependent samples - between the current and initial values. Statistically significant value was taken as $p < 0.05$.

For comparison of StO₂ values obtained by DOS and vascular fraction values obtained by OA with RHF and amounts of CD31 values obtained by IHC the Spearman correlation coefficient was calculated.

3. Results

Tumor models appeared to have different growth characteristics (Fig. 2). The growth rate of HCT116 and Colo320 significantly exceed that of SN-12C (Fig. 2(a)). The tumor volume doubling time was 5.1 ± 0.7 days and 4.9 ± 0.5 days respectively, while the same indicator for SN-12C was 13.6 ± 4.8 days (Fig. 2(b)). Statistically significant differences in the values of this parameter for SN-12C were found both for Colo320 ($p < 0.01$) and HCT116 ($p < 0.01$).

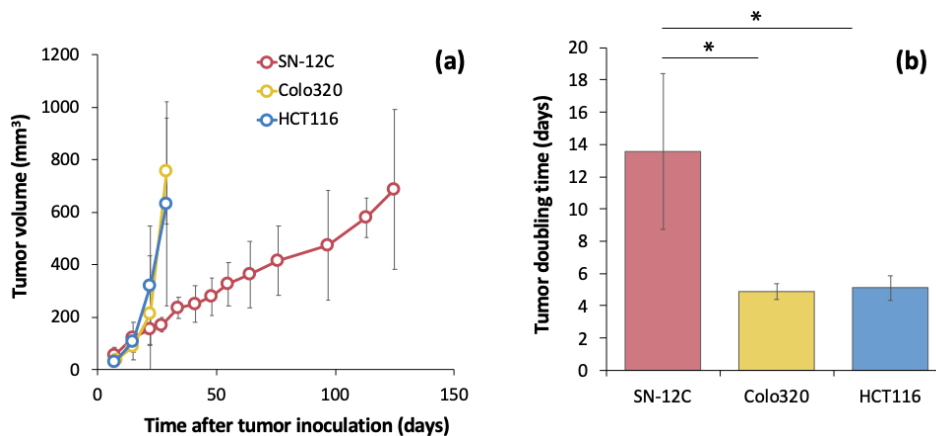


Fig. 2. Growth dynamics (a) and tumor doubling time (b) of SN-12C, Colo320, HCT116 tumors. $M \pm SD$, * - statistically significant differences between tumor models ($p < 0.05$, one-way ANOVA with Bonferroni correction)

The examples of OA images of normal and tumor vasculature are shown in Figs. 3–4. As compared to normal tissue, which is characterized by a regular arrangement of vessels (Fig. 3(a)), all investigated tumor xenografts were visualized as areas with a large number of tortuous, unevenly distributed vessels, which form areas of high and low vascularization (Fig. 4(a)). Due to the limited depth of the field of OA probe, vessels of normal tissues surrounding the tumors were visible until the tumor height exceeded 2 mm. The gradual increase of vascularization of the tumors was revealed with the tumor growth, however the features of the rate of the vascular network formation for different models were found (Fig. 4).

At the 7-th day after tumor inoculation the vascular fraction values of all tumor xenografts (Fig. 4(b)) were lower than those of normal tissues more than three times (Table 1). As the tumor volumes reached 700 mm³ Colo320 showed changes of vascular fraction from $2.8 \pm 0.6\%$ to $31.9 \pm 13.8\%$ by 29th day of growth, SN-12C - from $3.9 \pm 3.0\%$ to $29.1 \pm 4.7\%$ by 125th day of growth. The vascular fraction changed slightly in HCT116 from $3.0 \pm 2.2\%$ to $8.4 \pm 4.1\%$. It is worth noting the appearance of extensive hemoglobin-containing zones in Colo320 inside the tumor: the size increased by 16 times by the last day of tumor node growth and reached

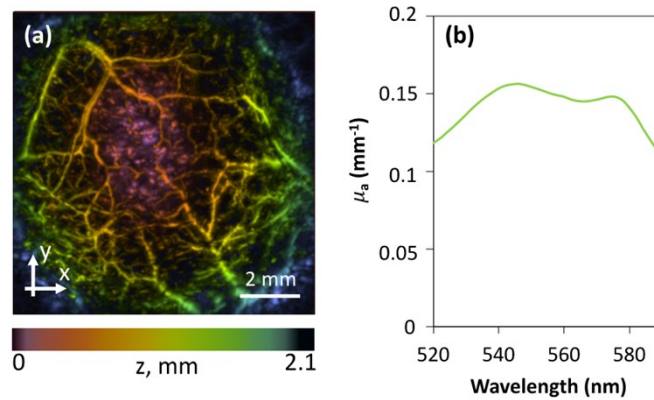


Fig. 3. Examples of OA image of vasculature (a) and DOS absorption spectra (b) of mouse normal tissues. The color scale codes the depth of the vessels.

$9.6 \times 10^4 \pm 6.8 \times 10^4 \mu\text{m}^2$. The same changes were less significant for HCT116 and SN-12C, 3 and 6 times respectively (Fig. 4(c)).

Table 1. Vascular fraction and vessels size obtained by OA, hemoglobin concentration and blood oxygen saturation level obtained by DOS for mouse normal tissue.

Optoacoustic imaging			
Vascular fraction (%)		Vessels size (μm^2)	
14.3 ± 3.9		$7.5 \times 10^3 \pm 3.6 \times 10^3$	
Diffuse Optical Spectroscopy			
tHb (μM)	HHb (μM)	HbO ₂ (μM)	StO ₂ (%)
22.8 ± 3.9	13.8 ± 3.5	8.7 ± 1.6	40.2 ± 6.5

Vessels size of tumors exceeded those for normal tissue (Table 1) by the 7th day for Colo320 growth, 22nd day for HCT116 growth, 29th day for SN-12C growth. Statistically significant differences with normal tissue were revealed for Colo320 ($p < 0.01$). Examples of the optical absorption coefficient spectra of normal tissue and tumors obtained by DOS are shown in Figs. 3 and 5. At the beginning of the monitoring tumor absorption spectra were similar for all the investigated models (Fig. 5(a)) and did not differ significantly from absorption spectra of normal tissue (Fig. 3(b)), suggesting similar chromophore content. When tumors reached the volume of 700 mm³ (last day of experiment), the shape of the Colo320 spectrum differed from the shape of the spectra of SN-12C and HCT116 demonstrated predominant deoxyhemoglobin content (Fig. 5(b)). For SN-12C and HCT116 tumors, the shape of the optical absorption spectrum changed insignificantly. According to DOS data, the drop in the level of blood oxygen saturation occurred in all tumor models (Fig. 5(c)).

During monitoring, the changes of StO₂ were revealed for HCT116 (from $52.0 \pm 11.3\%$ to $42.8 \pm 15.4\%$), for SN-12C (from $58.9 \pm 6.3\%$ to $33.2 \pm 12.0\%$), and for Colo320 (from $38.9 \pm 12.0\%$ to $17.7 \pm 7.8\%$). The most rapid and significant decrease in saturation was observed for Colo320. On the last day of the experiment significant differences in total hemoglobin levels (Fig. 5(e)) were found for Colo320 and SN-12C ($30.7 \pm 8.1 \mu\text{M}$ and $18.4 \pm 2.3 \mu\text{M}$ respectively). The decrease of HbO₂ concentration was observed in all tumor models to varying degrees (Fig. 5(f)). The decrease of HbO₂ was negligible for HCT116, while for Colo320 and SN-12C it was reduced by half. Colo320 was characterized by the largest change in the HHb (from

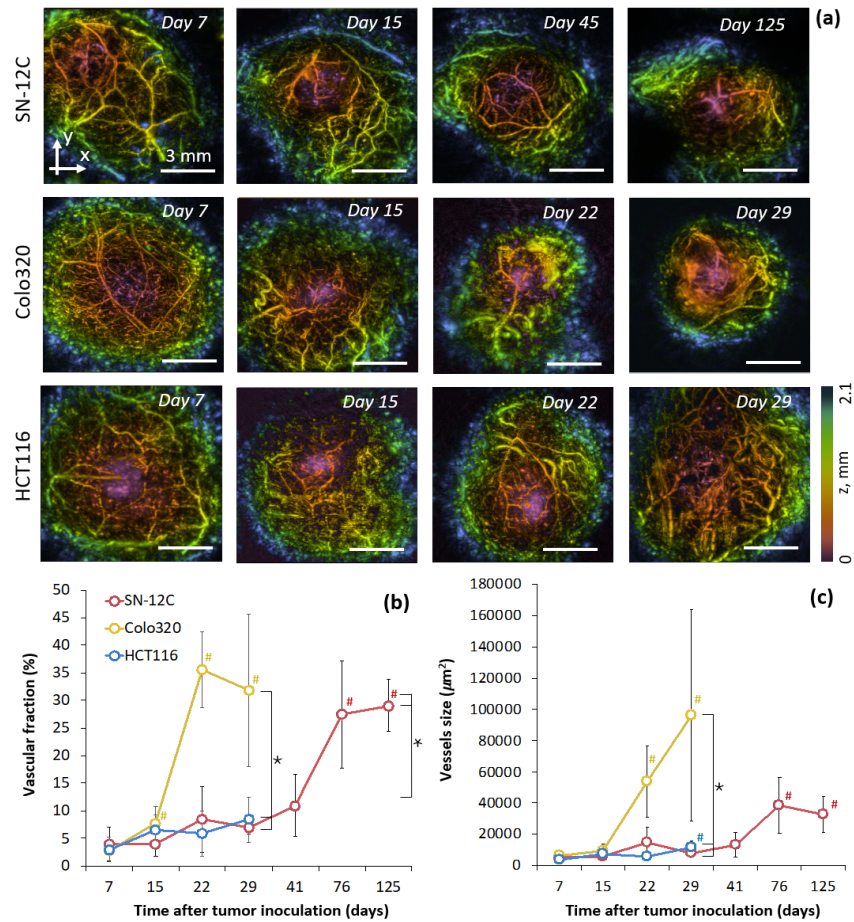


Fig. 4. OA images of vasculature (a), dynamics of vascular fraction (b) and vessels size (c) of SN-12C, Colo320, HCT116 tumors at different time points of their growth. The color scale codes the depth of the vessels. $Z = 0$ mm corresponds to the animal's surface. Bar - 3 mm. $M \pm SD$, * - statistically significant differences between tumor models ($p < 0.05$, one-way ANOVA with Bonferroni correction). # - statistically significant differences between current and baseline values ($p < 0.05$, t-test for dependent samples)

$17.1 \pm 4.5 \mu\text{M}$ to $25.7 \pm 8.8 \mu\text{M}$) (Fig. 5(d)). As compared to normal tissues (Table 1), decisive increase of tHb and HHb concentration was reached only for Colo320 ($p = 0.03$ and $p = 0.04$ respectively).

Figure 6 shows the examples of microimages of sections tumors after IHC staining (Fig. 6(a)) and the number of CD31 + microvessels per mm^2 (Fig. 6(b)) of SN-12C, Colo320, HCT116.

IHC study with antibodies to mouse endothelial cell marker CD31 revealed the following values for SN12C – 71.3 ± 11.9 , Colo320 – 90.4 ± 5.2 , HCT116 – 43.2 ± 7.3 . When comparing the vascular fraction values obtained by OA with the amounts of CD31 values obtained by IHC (Fig. 8(a)), a strong positive correlation $r = 0.7$ ($p < 0.05$) was revealed.

Immunofluorescent staining for hypoxia with pimonidazole revealed a difference in the hypoxia areas between the models (Fig. 7) with brightened pimonidazole-positive zones (Fig. 7(a)). In Colo320 the areas of hypoxic regions were larger as compared to other investigated models; RHF averaged value for Colo320 was $42.6 \pm 12.8\%$ and exceeded those for HCT116 and SN-12C by

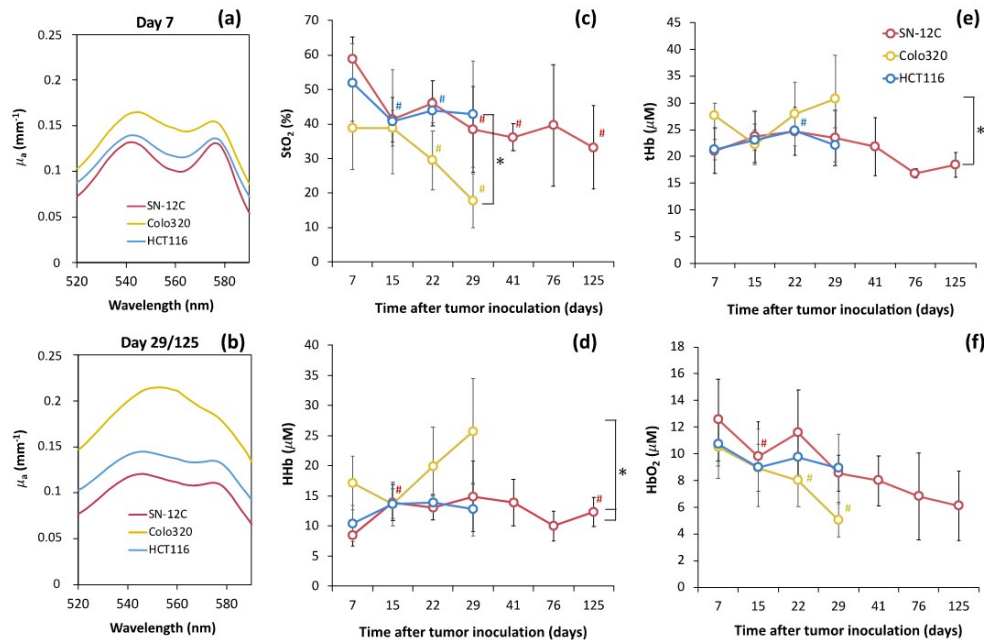


Fig. 5. DOS monitoring of SN-12C, Colo320, HCT116 tumors: typical reconstructed spectra of absorption coefficient at the 7th (a) and 29/125th days of tumor growth then the tumors reached 700 mm³ in average (b); blood oxygen saturation level (StO₂, c), deoxyhemoglobin (HHb, b), total hemoglobin (tHb, d), oxyhemoglobin (HbO₂, c) of tumors on different days of growth. M ± SD, * - statistically significant differences between tumor models (p < 0.05, one-way ANOVA with Bonferroni correction). # - statistically significant differences between current and baseline values (p < 0.05, t-test for dependent samples)

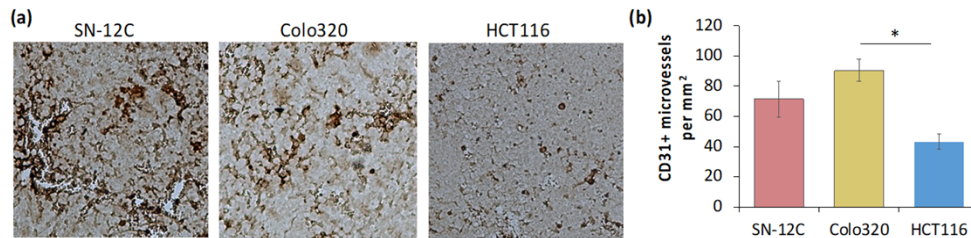


Fig. 6. Examples of microimages of sections (a) and the number of CD31 + microvessels (b) of SN-12C, Colo320, HCT116 tumors after immunohistochemical staining. M ± SD. * - statistically significant differences between tumor models (p < 0.05, one-way ANOVA with Bonferroni correction).

1.7 and 1.4 times, respectively. When comparing the StO₂ values obtained by DOS with the RHF values obtained by IHC with pimonidazole (Fig. 8(b)), a moderate negative correlation was revealed $r = -0.6$ ($p < 0.05$). Comparison of the values of vascular fraction and RHF shows only insignificant positive correlation (Fig. 8(c)).

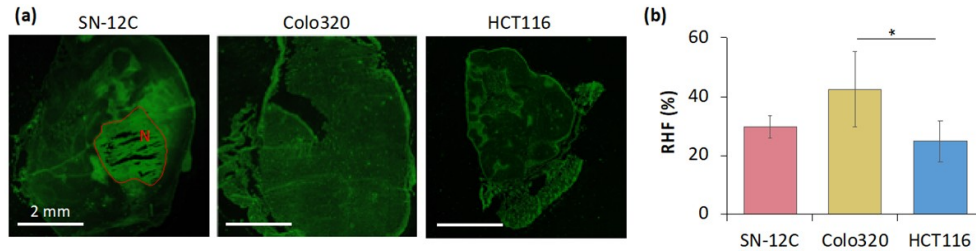


Fig. 7. Examples of LSM images of sections (a) and relative hypoxic fraction (RHF, b) of SN-12C, Colo320, HCT116 tumors after immunofluorescent staining for hypoxia with pimonidazole. N - necrosis zone. Bar - 2 mm. M \pm SD. * - statistically significant differences between tumor models ($p = 0.05$, one-way ANOVA with Bonferroni correction)

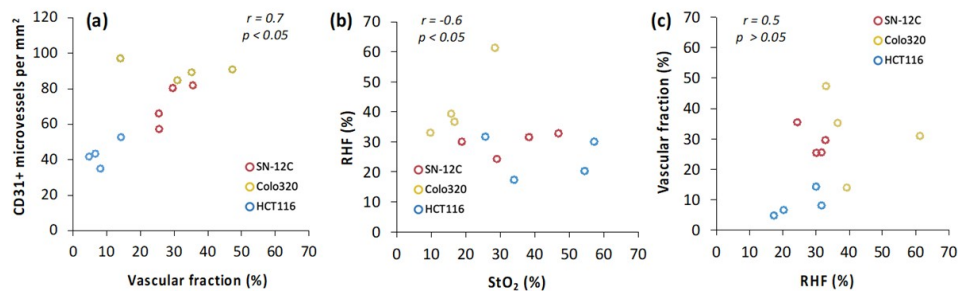


Fig. 8. Values of CD31 + microvessels versus vascular fraction (a), RHF versus StO₂ (b), vascular fraction versus RFP (c) for all mice (r is the Spearman correlation coefficient)

4. Discussion

The study of changes of vascularization and oxygenation is necessary both for understanding the mechanisms of formation of tumor hypoxia and for development of a new diagnostic and prognostic criteria for oncological diseases, as well as for substantiation of new therapeutic approaches that affect the vascular component of the tumor.

The possibilities of various imaging methods for comparing the qualitative and quantitative signs of the vascular bed of experimental neoplasms have already been studied in a number of works. In particular, the X-ray micro-computed tomography method revealed differences in such parameters as relative blood volume *in vivo* as well as vessel diameters and percentage of branches *ex vivo* between xenografts A431, Calu-6, MLS, and A549 [35]. Using dynamic contrast-enhanced ultrasonography, quantitative data on the vascularity of rat hepatomas based on three different cell lines are provided [36]. The method of optoacoustic imaging compared the vascularization of models of colon cancer [37,38].

Various non-invasive methods for determining the oxygenation level have also been used to assess the ability to determine the individual features of experimental neoplasms in comparative studies. The distribution of the novel tracer ¹⁸F-labeled pimonidazole was used to compare C3H and SCCVII hypoxia sites by PET *in vivo* [39]. The DOS method in the transillumination

configuration made it possible to reveal differences in the hemoglobin content and blood oxygen saturation of rat tumors [40].

Both methods independently have been already validated by several standard approaches. Our previous works had verified the DOS results using direct pO₂ measurements [41] and IHC analysis with pimonidazole, where a high percentage of hypoxia-positive zones confirmed the low content of oxyhemoglobin in tissues [40]. Tomaszewski et al. found a strong inverse correlation between optical tomography (OT) data and the level of hypoxia with Carbonic anhydrase IX. Moreover, the group used pimonidazole to determine the extent of tumor necrosis, which also demonstrated a strong inverse correlation with OT [42]. Optoacoustic angiography was independently compared to hematoxylin-eosin staining and IHC for endothelial marker CD31 [43], and α -smooth muscle actin [44], which allow assessing both the structure of the tumor tissue and the formation of the vasculature.

It should be noted that acoustic resolution OA can be used for the averaged assessment of blood oxygen saturation as an independent method. Using this approach, numerous studies have investigated changes in the oxygenation of tumor models during growth and under treatment [45–48] and performed the comparison of oxygen state of different tumor models [49]. For high-precision OA measurements of saturation at pre-diffuse depths, OA microscopes of the so-called optical resolution have proven well [50].

We used the experience of other groups for structural diagnostics (angiography), where we supplemented an acoustic resolution OA scanning system that performs diffuse laser illumination of vessels at 532 nm with the DOS system in a diffuse mode. The similar optical wavelengths and illumination geometry we used in the technical implementation of the DOS application cause and detect complementary saturation measurements in a volume measurement similar to OA. This combination of methods worked well in our previous research [20].

In our study we compared several tumor models and revealed both similar features for all neoplasms that distinguish them from normal tissues, as well as individual features of the development of the vascular network of each type of tumor. In comparison with normal tissues the loss of regular distribution and increased tortuosity of the vessels were the unite features according to the data of OA. However, each model studied had its own individual differences, which increased with the growth of the neoplasm. The rapidly growing HCT116 tumor during the monitoring period did not show a significant increase in the fraction of vessels and changes in their size; according to OA angiography, these parameters remained comparable to the normal tissues (Fig. 4). For this model, the smallest decrease in blood oxygen saturation compared to the initial level was shown among all the studied ones (Fig. 5).

Another rapidly growing tumor, Colo320, on the contrary, was characterized by a very rapid increase in the vascular fraction and a significant expansion of hemoglobin-containing zones (16-fold). These changes were accompanied by a rapid accumulation of hemoglobin and the most significant decrease in oxygenation of all models.

The slowly growing SN-12C tumor by the end of the experiment showed a significant increase in the values of the vascular fraction, while the size of hemoglobin-containing structures increased slightly, which indicates the absence of extensive hemorrhages and the formation of a large number of vascular structures. The blood supply of this model did not undergo significant changes, and blood oxygen saturation decreased significantly compared to the initial level, nevertheless remaining higher than that of Colo320.

An IHC study with antibodies to the endothelial cell marker CD31 demonstrated more CD31 in Colo320 and SN-12C compared to HCT116, at the same time, some areas with hemorrhages in the tumor tissue do not have a vascular lining and represent destroyed vessels. Good correspondence was revealed between values of vascular fraction obtained by OA and values of CD31 + microvessels obtained by IHC (Fig. 4, 6, 8). The results of IHC analysis of tissue samples with a marker of hypoxia correlate well with the results of the DOS study, demonstrating

the highest values of the relative hypoxic fraction for the Colo320 model and the lowest level of StO₂ compared to other models (Fig. 5, 7, 8).

A moderate negative correlation was found between the saturation values and the area of pimonidazole-positive zones of the studied tumors. Our results on the degree of vascularization of the studied tumors are consistent with data [51], demonstrating a fourfold excess of CD31 in Colo320 compared to HCT116, explained in the work by higher expression of PROK2. A comparative study of metastatic and primary CRC series (including Colo320 and HCT116) revealed no significant difference in VEGF expression in normoxia. No expression of VEGFR-2 was detected in CRC cell lines, and expression of sVEGFR-1 was independent of the cellular origin of CRC [52].

Tissue oxygenation is determined by oxygen supply, outflow and consumption. Changes in the concentration of oxy- and deoxyhemoglobin may indirectly reflect the mechanisms of changes in blood oxygen saturation [53,54]. In our present work, DOS revealed that in Colo320 the StO₂ decrease is determined by both accumulation of deoxyhemoglobin and drop of oxyhemoglobin concentration. Considering the rapid growth and extensive hemorrhages found by OA in this tumor model, high oxygen consumption with a low outflow rate of oxygen-depleted blood can be assumed (Fig. 5(d)). At the same time, the newly formed tumor vascular system probably cannot cope with the supply of oxygen to the neoplasm cells (Fig. 5(f)). In SN-12C and HCT116, the drop in saturation is predominantly determined a decrease in oxyhemoglobin levels, demonstrating a decrease in oxygen supply as the main cause of the decrease in oxygenation.

Comparison of IHC data with pimonidazole and OA data (Fig. 8(c)) showed that the relative hypoxic fraction increases with increasing vascular fraction. Moreover, the highest values of both parameters were found for Colo320, the lowest - for HCT116. It should be noted that vascular fraction is considered as the area occupied by hemoglobin in OA images and consists of both intact vessels and hemorrhages. Therefore, hemorrhage area has a greater contribution to the values of vascular fraction than oxygen-carrying vessel area that may be considered as the reason for the low level of oxygenation in Colo320 compared to other models.

It is known that the level of oxygenation of neoplasms is determined by the state of the vascular bed, and the slower the vessels develop, the less they satisfy the oxygen needs of tumor cells [55,56]. One of the main molecular mechanisms that are activated under conditions of reduced tissue oxygenation is the stimulation of neoangiogenesis with an increase in the expression of vascular endothelial growth factor [57]. Thus, hypoxia stimulates angiogenesis, that leads to further tumor growth and requires the further formation of new tumor vessels. In SN-12C, vascular growth doesn't begin immediately, but only after 41 days of monitoring, while the decrease in oxygenation begins as early as 15 days of tumor growth. The earlier changes in oxygenation compared to vascular growth in this tumor model may be one of the indicators for the involvement of hypoxia in the stimulation of vascular growth. However, for the Colo320 model, an increase in the vascular fraction occurred simultaneously with a decrease in saturation. Apparently, the formation of defective and presumably fluid vessels could not cope with the delivery of oxygen despite a significant increase in the blood supply of the neoplasm.

5. Conclusion

We compared structural and functional parameters of the vascular bed of experimental tumors of various morphogenesis. The combination of non-invasive methods of DOS and OA allows simultaneous assessment of changes in blood content, blood oxygen saturation, track changes in the number and shape of vessels in pre-clinical models of cancer. During growth up to the similar volume, the comparable increase of vascularity was revealed for Colo320 and SN12C, for HCT116 the changes were insignificant. Colo320 was found to form extensive hemoglobin-containing structures as the tumor node grows. Such data may indicate the formation of hemorrhages. DOS revealed a gradual decrease in oxygenation during the growth of all experimental tumors; however,

Colo320 is characterized by the most rapid decline. The possibilities of combination of methods of OA and DOS for monitoring of vessel growth, for identifying the features of blood vessel structure and their influence on oxygenation of various tumor models have been demonstrated. This approach may be useful for assessment of the tumor vascular response to different types of treatment.

Funding. Russian Science Foundation (21-15-00032).

Acknowledgements. The authors are grateful to Prof. Vladimir Vodeneev, Dr. Marina Sirotkina and Dr. Anna Brilkina for valuable contribution to the discussions; to Dr. Mikhail Kleshnin for assistance in DOS measurements; to Dr. Marina Karabut, Dr. Eliso Solomko, Olga Kutova and Aleksandra Bogomolova for assistance in IHC analysis; to Andrey Kovalchuk for Matlab GUI for automated OA scanning and to Alexander Khilov for Matlab GUI for automated data processing; to Vladimir Vorobjev, Maksim Prudnikov and Roman Belyaev for engineering contribution to this work.

Disclosures. The authors declare that there are no conflicts of interest related to this article.

Data availability. Data underlying the results presented in this paper are not publicly available at this time but may be obtained from the authors upon reasonable request.

References

1. B. Muz, P. de la Puente, F. Azab, and A. K. Azab, "The role of hypoxia in cancer progression, angiogenesis, metastasis, and resistance to therapy," *Hypoxia* **3**, 83 (2015).
2. J. M. Brown and W. R. Wilson, "Exploiting tumour hypoxia in cancer treatment," *Nat. Rev. Cancer* **4**(6), 437–447 (2004).
3. P. Vaupel and L. Harrison, "Tumor hypoxia: causative factors, compensatory mechanisms, and cellular response," *The oncologist* **9**(S5), 4–9 (2004).
4. A. Eberhard, S. Kahlert, V. Goede, B. Hemmerlein, K. H. Plate, and H. G. Augustin, "Heterogeneity of angiogenesis and blood vessel maturation in human tumors: implications for antiangiogenic tumor therapies," *Cancer Res.* **60**(5), 1388–1393 (2000).
5. N. Nishida, H. Yano, T. Nishida, T. Kamura, and M. Kojiro, "Angiogenesis in cancer," *Vasc. Health Risk Manage.* **2**(3), 213–219 (2006).
6. C. Cai, X. Wang, Q. Fu, and A. Chen, "The VEGF expression associated with prognosis in patients with intrahepatic cholangiocarcinoma: a systematic review and meta-analysis," *World J. Surg. Onc.* **20**(1), 1–10 (2022).
7. B. Nico, V. Benagiano, D. Mangieri, N. Maruotti, A. Vacca, and D. Ribatti, "Evaluation of microvascular density in tumors, pro and contra," *Histology and histopathology* (2008).
8. D. M. McDonald and P. L. Choyke, "Imaging of angiogenesis: from microscope to clinic," *Nat. Med.* **9**(6), 713–725 (2003).
9. V. Ntziachristos and B. Chance, "Breast imaging technology: Probing physiology and molecular function using optical imaging-applications to breast cancer," *Breast Cancer Res.* **3**(1), 41 (2000).
10. T. Durduran, R. Choe, W. B. Baker, and A. G. Yodh, "Diffuse optics for tissue monitoring and tomography," *Rep. Prog. Phys.* **73**(7), 076701 (2010).
11. K. Vishwanath, H. Yuan, W. T. Barry, M. W. Dewhirst, and N. Ramanujam, "Using optical spectroscopy to longitudinally monitor physiological changes within solid tumors," *Neoplasia* **11**(9), 889–900 (2009).
12. A. Orlova, A. Maslennikova, G. Y. Golubiatnikov, A. Suryakova, M. Y. Kirillin, D. Kurakina, T. Kalganova, A. Volovetsky, and I. Turchin, "Diffuse optical spectroscopy assessment of rodent tumor model oxygen state after single-dose irradiation," *Biomed. Phys. Eng. Express* **5**(3), 035010 (2019).
13. C. Zhou, R. Choe, N. S. Shah, T. Durduran, G. Yu, A. Durkin, D. Hsiang, R. Mehta, J. A. Butler, and A. E. Cerussi, "Diffuse optical monitoring of blood flow and oxygenation in human breast cancer during early stages of neoadjuvant chemotherapy," *J. Biomed. Opt.* **12**(5), 051903 (2007).
14. M. V. Pavlov, T. I. Kalganova, Y. S. Lyubimtseva, V. I. Plekhanov, G. Y. Golubyatnikov, O. Y. Ilyinskaya, A. G. Orlova, P. V. Subochev, D. V. Safonov, and N. M. Shakhova, "Multimodal approach in assessment of the response of breast cancer to neoadjuvant chemotherapy," *J. Biomed. Opt.* **23**(09), 1 (2018).
15. Y. Zhang, A. J. Moy, X. Feng, H. T. Nguyen, J. S. Reichenberg, M. K. Markey, and J. W. Tunnell, "Physiological model using diffuse reflectance spectroscopy for nonmelanoma skin cancer diagnosis," *J. Biophotonics* **12**(12), e201900154 (2019).
16. J.-T. Oh, M.-L. Li, H. F. Zhang, K. Maslov, and L. V. Wang, "Three-dimensional imaging of skin melanoma in vivo by dual-wavelength photoacoustic microscopy," *J. Biomed. Opt.* **11**(3), 034032 (2006).
17. A. B. E. Attia, S. Y. Chuah, D. Razansky, C. J. H. Ho, P. Malempati, U. Dinis, R. Bi, C. Y. Fu, S. J. Ford, and J. S.-S. Lee, "Noninvasive real-time characterization of non-melanoma skin cancers with handheld optoacoustic probes," *Photoacoustics* **7**, 20–26 (2017).
18. H. Ma, S. Yang, Z. Cheng, and D. Xing, "Photoacoustic confocal dermoscope with a waterless coupling and impedance matching opto-sono probe," *Opt. Lett.* **42**(12), 2342–2345 (2017).

19. K. Haedicke, L. Agemy, M. Omar, A. Berezhnoi, S. Roberts, C. Longo-Machado, M. Skubal, K. Nagar, H.-T. Hsu, and K. Kim, "High-resolution optoacoustic imaging of tissue responses to vascular-targeted therapies," *Nat. Biomed. Eng.* **4**(3), 286–297 (2020).
20. A. Orlova, K. Pavlova, A. Kurnikov, A. Maslennikova, M. Myagcheva, E. Zakharov, D. Skamnitskiy, V. Perekatova, A. Khilov, and A. Kovalchuk, "Noninvasive optoacoustic microangiography reveals dose and size dependency of radiation-induced deep tumor vasculature remodeling," *Neoplasia* **26**, 100778 (2022).
21. N. Fowlkes, K. Clemons, P. J. Rider, R. Subramanian, N. Wakamatsu, I. Langohr, and K. G. Kousoulas, "Factors affecting growth kinetics and spontaneous metastasis in the B16F10 syngeneic murine melanoma model," *Comp. Med.* **69**(1), 48–54 (2019).
22. G. J. Greening, K. P. Miller, C. R. Spainhour, M. D. Cato, and T. J. Muldoon, "Effects of isoflurane anesthesia on physiological parameters in murine subcutaneous tumor allografts measured via diffuse reflectance spectroscopy," *Biomed. Opt. Express* **9**(6), 2871–2886 (2018).
23. P. Subochev, "Cost-effective imaging of optoacoustic pressure, ultrasonic scattering, and optical diffuse reflectance with improved resolution and speed," *Opt. Lett.* **41**(5), 1006–1009 (2016).
24. U. A. Hofmann, J. Rebling, H. Estrada, P. Subochev, and D. Razansky, "Rapid functional optoacoustic microangiography in a burst mode," *Opt. Lett.* **45**(9), 2522–2525 (2020).
25. A. Kurnikov, K. Pavlova, A. G. Orlova, A. V. Khilov, V. Perekatova, A. Kovalchuk, and P. V. Subochev, "Broadband (100 kHz–100 MHz) ultrasound PVDF detectors for raster-scan optoacoustic angiography with acoustic resolution," *Quantum Electron.* **51**(5), 383–388 (2021).
26. W. Li, U. A. Hofmann, J. Rebling, Q. Zhou, Z. Chen, A. Ozbek, Y. Gong, P. Subochev, D. Razansky, and X. L. Deán-Ben, "Broadband Model-Based Optoacoustic Mesoscopy Enables Deep-Tissue Imaging beyond the Acoustic Diffraction Limit," *Laser Photonics Rev.* **16**(5), 2100381 (2022).
27. P. Subochev, E. Smolina, E. Sergeeva, M. Kirillin, A. Orlova, D. Kurakina, D. Emyanov, and D. Razansky, "Toward whole-brain in vivo optoacoustic angiography of rodents: modeling and experimental observations," *Biomed. Opt. Express* **11**(3), 1477–1488 (2020).
28. B. E. Treeby and B. T. Cox, "k-Wave: MATLAB toolbox for the simulation and reconstruction of photoacoustic wave fields," *J. Biomed. Opt.* **15**(2), 021314 (2010).
29. P. Subochev, F. Spadin, V. Perekatova, A. Khilov, A. Kovalchuk, K. Pavlova, A. Kurnikov, M. Frenz, and M. Jaeger, "Toward Real-Time Giga-Voxel Optoacoustic/Photoacoustic Microscopy: GPU-Accelerated Fourier Reconstruction with Quasi-3D Implementation," in *Photonics (MDPI2021)*, p. 15.
30. M. S. Kleshnin and I. V. Turchin, "Evaluation of oxygenation in the surface layers of biological tissues based on diffuse optical spectroscopy with automated calibration of measurements," *Quantum Electron.* **49**(7), 628–632 (2019).
31. A. Orlova, Y. Perevalova, K. Pavlova, N. Orlinskaya, A. Khilov, D. Kurakina, M. Shakhova, M. Kleshnin, E. Sergeeva, and I. Turchin, "Diffuse Optical Spectroscopy Monitoring of Experimental Tumor Oxygenation after Red and Blue Light Photodynamic Therapy," in *Photonics (MDPI2021)*, p. 19.
32. M. S. Kleshnin, "Deep learning neural network estimation of tissue oxygenation based on diffuse optical spectroscopy," *Laser Phys.* **29**(8), 085603 (2019).
33. J. Raleigh, S. Chou, G. Arteel, and M. Horsman, "Comparisons among pimonidazole binding, oxygen electrode measurements, and radiation response in C₃H mouse tumors," *Radiat. Res.* **151**(5), 580–589 (1999).
34. R. A. Cairns, I. Papandreou, P. D. Sutphin, and N. C. Denko, "Metabolic targeting of hypoxia and HIF1 in solid tumors can enhance cytotoxic chemotherapy," *Proc. Natl. Acad. Sci.* **104**(22), 9445–9450 (2007).
35. J. Ehling, B. Theek, F. Gremse, S. Baetke, D. Möckel, J. Maynard, S.-A. Ricketts, H. Grüll, M. Neeman, and R. Knuechel, "Micro-CT imaging of tumor angiogenesis: quantitative measures describing micromorphology and vascularization," *Am. J. Pathol.* **184**(2), 431–441 (2014).
36. J. W. Choi, J. H. Kim, H.-C. Kim, W. S. Choi, S. Y. Baek, K. Lee, and J. W. Chung, "Comparison of tumor vascularity and hemodynamics in three rat hepatoma models," *Abdom. Radiol.* **41**(2), 257–264 (2016).
37. J. G. Laufer, E. Z. Zhang, B. E. Treeby, B. T. Cox, P. C. Beard, P. Johnson, and B. Pedley, "In vivo preclinical photoacoustic imaging of tumor vasculature development and therapy," *J. Biomed. Opt.* **17**(5), 056016 (2012).
38. A. Orlova, M. Sirotkina, E. Smolina, V. Elagin, A. Kovalchuk, I. Turchin, and P. Subochev, "Raster-scan optoacoustic angiography of blood vessel development in colon cancer models," *Photoacoustics* **13**, 25–32 (2019).
39. M. Busk, S. Jakobsen, M. R. Horsman, L. S. Mortensen, A. B. Iversen, J. Overgaard, M. Nordsmark, X. Ji, D. Y. Lee, and J. R. Raleigh, "PET imaging of tumor hypoxia using 18F-labeled pimonidazole," *Acta Oncol.* **52**(7), 1300–1307 (2013).
40. A. V. Maslennikova, A. G. Orlova, G. Y. Golubiatnikov, V. A. Kamensky, N. M. Shakhova, A. A. Babaev, L. B. Snopova, I. P. Ivanova, V. I. Plekhanov, and T. I. Prianikova, "Comparative study of tumor hypoxia by diffuse optical spectroscopy and immunohistochemistry in two tumor models," *J. Biophotonics* **3**(12), 743–751 (2010).
41. A. G. Orlova, M. Y. Kirillin, A. B. Volovetsky, N. Y. Shilyagina, E. A. Sergeeva, G. Y. Golubiatnikov, and I. V. Turchin, "Diffuse optical spectroscopy monitoring of oxygen state and hemoglobin concentration during SKBR-3 tumor model growth," *Laser Phys. Lett.* **14**(1), 015601 (2017).
42. M. R. Tomaszewski, M. Gehrunge, J. Joseph, I. Quiros-Gonzalez, J. A. Disselhorst, and S. E. Bohndiek, "Oxygen-enhanced and dynamic contrast-enhanced optoacoustic tomography provide surrogate biomarkers of tumor vascular function, hypoxia, and necrosis," *Cancer Res.* **78**(20), 5980–5991 (2018).

43. I. Turchin, Sh. Bano, M. Kirillin, A. Orlova, V. Perekatova, V. Plekhanov, E. Sergeeva, D. Kurakina, A. Khilov, A. Kurnikov, P. Subochev, M. Shirmanova, A. Komarova, D. Yuzhakova, A. Gavrina, S. Mallidi, and T. Hasan, "Combined Fluorescence and Optoacoustic Imaging for Monitoring Treatments against CT26 Tumors with Photoactivatable Liposomes," *Cancers* **14**(1), 197 (2021).
44. E. L. Brown, T. L. Lefebvre, P. W. Sweeney, B. J. Stolz, J. Gröhl, L. Hacker, Z. Huang, D.-L. Couturier, H. A. Harrington, H. M. Byrne, and S. E. Bohndiek, "Quantification of vascular networks in photoacoustic mesoscopy," *Photoacoustics* **26**, 100357 (2022).
45. M. Gerling, Y. Zhao, S. Nania, K. J. Norberg, C. S. Verbeke, B. Englert, R. V. Kuiper, Å. Bergström, M. Hassan, and A. Neesse, "Real-time assessment of tissue hypoxia in vivo with combined photoacoustics and high-frequency ultrasound," *Theranostics* **4**(6), 604–613 (2014).
46. V. Neuschmelting, K. Kim, J. Malekzadeh-Najafabadi, S. Jebiwott, J. Prakash, A. Scherz, J. A. Coleman, M. F. Kircher, and V. Ntziachristos, "WST11 vascular targeted photodynamic therapy effect monitoring by multispectral optoacoustic tomography (MSOT) in mice," *Theranostics* **8**(3), 723–734 (2018).
47. P. Ghosh, Y. Guo, A. Ashrafi, J. Chen, S. Dey, S. Zhong, J. Liu, J. Campbell, P. C. Konduri, and J. Gerberich, "Oxygen-enhanced optoacoustic tomography reveals the effectiveness of targeting heme and oxidative phosphorylation at normalizing tumor vascular oxygenation," *Cancer Res.* **80**(17), 3542–3555 (2020).
48. E. Liapis, A. Karlas, U. Klemm, and V. Ntziachristos, "Chemotherapeutic effects on breast tumor hemodynamics revealed by eigenspectra multispectral optoacoustic tomography (eMSOT)," *Theranostics* **11**(16), 7813–7828 (2021).
49. I. Quiros-Gonzalez, M. R. Tomaszewski, S. J. Aitken, L. Ansel-Bollepalli, L.-A. McDuffus, M. Gill, L. Hacker, J. Brunker, and S. E. Bohndiek, "Optoacoustics delineates murine breast cancer models displaying angiogenesis and vascular mimicry," *Br. J. Cancer* **118**(8), 1098–1106 (2018).
50. X. Zhu, Q. Huang, A. DiSpirito, T. Vu, Q. Rong, X. Peng, H. Sheng, X. Shen, Q. Zhou, and L. Jiang, "Real-time whole-brain imaging of hemodynamics and oxygenation at micro-vessel resolution with ultrafast wide-field photoacoustic microscopy," *Light: Sci. Appl.* **11**(1), 1–15 (2022).
51. H. Kurebayashi, T. Goi, M. Shimada, N. Tagai, T. Naruse, T. Nakazawa, Y. Kimura, Y. Hirono, and A. Yamaguchi, "Prokineticin 2 (PROK2) is an important factor for angiogenesis in colorectal cancer," *Oncotarget* **6**(28), 26242–26251 (2015).
52. A. Abajo, N. Bitarte, R. Zarate, V. Boni, I. Lopez, M. Gonzalez-Huarriz, J. Rodriguez, E. Bandres, and J. Garcia-Foncillas, "Identification of colorectal cancer metastasis markers by an angiogenesis-related cytokine- antibody array," *World J. Gastroenterology: WJG* **18**(7), 637 (2012).
53. R. A. De Blasi, M. Cope, C. Elwell, F. Safoue, and M. Ferrari, "Noninvasive measurement of human forearm oxygen consumption by near infrared spectroscopy," *Eur. J. Appl. Physiol. Occup. Physiol.* **67**(1), 20–25 (1993).
54. H. Lu, X. Golay, J. J. Pekar, and P. C. Van Zijl, "Sustained poststimulus elevation in cerebral oxygen utilization after vascular recovery," *J. Cereb. Blood Flow Metab.* **24**(7), 764–770 (2004).
55. M. Plank and B. Sleeman, "Tumour-induced angiogenesis: a review," *J. Theoretical Med.* **5**(3-4), 137–153 (2003).
56. P. Vaupel, A. Mayer, S. Briest, and M. Höckel, "Oxygenation gain factor: a novel parameter characterizing the association between hemoglobin level and the oxygenation status of breast cancers," *Cancer Res.* **63**(22), 7634–7637 (2003).
57. G. L. Semenza, "Cancer–stromal cell interactions mediated by hypoxia-inducible factors promote angiogenesis, lymphangiogenesis, and metastasis," *Oncogene* **32**(35), 4057–4063 (2013).